

# Adiabatic echo protocols for robust quantum many-body state preparation

Zhongda Zeng,<sup>1,2,\*</sup> Giuliano Giudici,<sup>1,2,\*</sup> Aruku Senoo,<sup>3</sup>

Alexander Baumgärtner,<sup>3</sup> Adam M. Kaufman,<sup>3</sup> and Hannes Pichler<sup>1,2,†</sup>

<sup>1</sup>*Institute for Theoretical Physics, University of Innsbruck, Innsbruck 6020, Austria*

<sup>2</sup>*Institute for Quantum Optics and Quantum Information, Austrian Academy of Sciences, Innsbruck 6020, Austria*

<sup>3</sup>*JILA, University of Colorado and National Institute of Standards and Technology, and Department of Physics, University of Colorado, Boulder, Colorado 80309, USA*

(Dated: June 17, 2025)

Entangled many-body states are a key resource for quantum technologies. Yet their preparation through analog control of interacting quantum systems is often hindered by experimental imperfections. Here, we introduce the adiabatic echo protocol, a general approach to state preparation designed to suppress the effect of static perturbations. We provide an analytical understanding of its robustness in terms of dynamically engineered destructive interference. By applying quantum optimal control methods, we demonstrate that such a protocol emerges naturally in a variety of settings, without requiring assumptions on the form of the control fields. Examples include Greenberger-Horne-Zeilinger state preparation in Ising spin chains and two-dimensional Rydberg atom arrays, as well as the generation of quantum spin liquid states in frustrated Rydberg lattices. Our results highlight the broad applicability of this protocol, providing a practical framework for reliable many-body state preparation in present-day quantum platforms.

**Introduction.** – High-fidelity preparation of many-body quantum states is essential for advancing quantum technologies, with applications ranging from quantum computation and simulation [1–7] to precision sensing [8–10]. Analog approaches provide a natural and well-established route via continuous steering of the system through time-dependent control fields [11–15]. However, their effectiveness is often limited by experimental imperfections, such as static perturbations that alter the system dynamics in an uncontrolled fashion, thereby reducing the fidelity with the target state [16]. This motivates the development of control protocols that not only drive the system toward the desired state, but also mitigate the detrimental effects of such imperfections to ensure reliable state preparation under realistic conditions.

We focus on the problem of preparing the ground state of a parameter-dependent Hamiltonian  $\hat{H}_0(s)$ , by evolving the system from the ground state at  $s_0$  to that at  $s_T$ , in the presence of a static perturbation  $\epsilon\hat{V}$  (cf. Fig. 1). Our goal is to devise control protocols that are robust to such static perturbations, i.e., insensitive to small variations in  $\epsilon$ , which is fixed during the evolution but may vary across experimental runs. To this end, we introduce a generic preparation strategy that emerges from optimal control [17] and can be implemented across a broad class of many-body Hamiltonians. We dub this protocol *adiabatic echo protocol*, as it operates by dynamically “echoing out” the effect of static perturbations during an adiabatic evolution. After outlining the general setting in which the protocol is applicable, we provide an analytical understanding of the mechanism behind its robustness. We then show how it naturally arises in concrete interacting models using the Gradient Ascent Pulse Engineering (GRAPE) algorithm [18]—a method

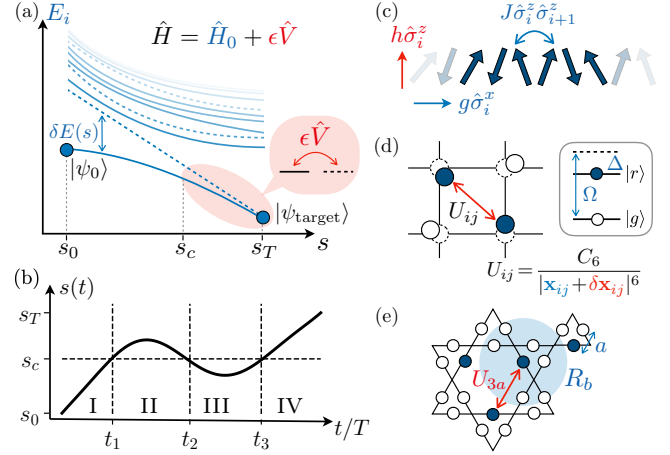


**Figure 1. Many-body adiabatic echo protocol.** (a) Spectrum of a many-body Hamiltonian  $\hat{H}_0(s)$  with  $\mathbb{Z}_2$  symmetry breaking. The initial and target states lie in the trivial and ordered phases, separated by a critical point  $s_c$ . Solid (dashed) lines indicate eigenenergies in the even (odd)  $\mathbb{Z}_2$  sectors. A perturbation  $\hat{V}$  breaks the symmetry and couples these sectors, affecting the dynamics for  $s > s_c$ , when the gap  $\delta E(s)$  is exponentially small with system size. (b) Illustration of the adiabatic echo protocol. Contributions to the infidelity  $\mathcal{I}$  from regions I and III vanish, while those from regions II and IV destructively interfere. (c–e) Applications where the echo protocol mitigates the effect of the perturbation  $\hat{V}$ : (c) Ising chain with transverse and longitudinal fields, (d) square lattice Rydberg array with positional disorder, (e) ruby lattice Rydberg array with long-range interactions.

widely used in few-qubit gate design [19–23] but rarely applied in the context of many-body state preparation. In particular, we showcase its versatility across various contexts, including Greenberger–Horne–Zeilinger (GHZ)

state preparation in the quantum Ising chain, as well as the generation of GHZ and quantum spin liquid (QSL) states in two-dimensional Rydberg atom arrays. We further confirm the benefits of the adiabatic echo protocol in a companion experimental work by preparing GHZ states in Rydberg atom ladders [24].

*Adiabatic echo protocol.* – Dynamical preparation of many-body states often relies on the adiabatic theorem, which ensures that a system governed by a Hamiltonian  $\hat{H}_0(s)$  remains close to its instantaneous ground state when a control parameter  $s(t)$  is varied slowly in time, relative to the inverse energy gap [15]. In this regime, the system can be driven with high fidelity from an initial, easy-to-prepare ground state  $|\psi_0\rangle$  at  $s(0) = s_0$  to a strongly correlated target ground state  $|\psi_{\text{target}}\rangle$  at  $s(T) = s_T$ . The buildup of quantum correlations in the target state typically requires crossing a phase transition, where the spectrum is gapless in the thermodynamic limit. For a continuous phase transition, this implies a preparation time that grows algebraically with system size to achieve a fixed fidelity [15].

In the simplest scenario, the phase transition occurs via spontaneous symmetry breaking (SSB), with a critical point  $s_c$  separating a trivial phase ( $s < s_c$ ) from an ordered phase ( $s > s_c$ ). The initial and final values of the control function,  $s_0$  and  $s_T$ , lie in the trivial and ordered phases, respectively. Below, we focus on  $\mathbb{Z}_2$  symmetry breaking and refer to [25] for a discussion of higher-order symmetry groups. The typical energy spectrum of a many-body Hamiltonian undergoing such a transition is sketched in Fig. 1a: for  $s < s_c$ , the ground state  $|E_0(s)\rangle$  is well separated from the excited states, while for  $s > s_c$ , SSB leads to an exponentially small gap between the ground state and the first excited state  $|E_1(s)\rangle$ . We assume that these two states belong to different  $\mathbb{Z}_2$  symmetry sectors for all  $s$ .

In the absence of perturbations, symmetry forbids mixing between  $|E_0(s)\rangle$  and  $|E_1(s)\rangle$ . However, static symmetry-breaking terms  $\epsilon\hat{V}$ —arising from experimental imperfections or theoretical approximations—induce a nonzero coupling  $V_{10}(s) = \langle E_1(s) | \hat{V} | E_0(s) \rangle$ . In the adiabatic limit, couplings to other higher excited states can be neglected, and the leading-order contribution to the preparation infidelity  $\mathcal{I} = 1 - |\langle \psi_{\text{target}} | \psi(T) \rangle|^2$  is given by time-dependent perturbation theory as [25]

$$\mathcal{I} = \epsilon^2 \left| \int_0^T dt V_{10}(s(t)) e^{-i \int_t^T d\tau \delta E(s(\tau))} \right|^2, \quad (1)$$

where  $\delta E(s) = E_1(s) - E_0(s)$  is the lowest energy gap.

The dominant contributions to the infidelity generically arise from the region where  $\delta E(s)$  is exponentially small with the system size  $L$  ( $s > s_c$ ), while contributions from the finite-gap region ( $s < s_c$ ) are subleading and parametrically suppressed with  $L$ . We neglect the latter contributions in the following and refer to [25] for a formal

justification of this approximation.

In a standard adiabatic protocol,  $s(t)$  is monotonic and the critical point  $s_c$  is crossed only once at  $t = t_c$ . Due to the exponentially small gap, the phase of the integrand in Eq. (1) simplifies, and the infidelity reduces to  $\mathcal{I} \simeq \epsilon^2 |V_{10}|^2 (T - t_c)^2$ , where we assumed  $V_{10}(s) \simeq V_{10}$ . Hence, while increasing the total evolution time  $T$  improves adiabaticity, it amplifies the infidelity in the presence of symmetry-breaking perturbations.

This trade-off can be avoided by protocols that sweep across the phase transition multiple times, such as the one in Fig. 1b, which consists of four segments. In segments I and III,  $s < s_c$ , while in II and IV,  $s > s_c$ . Neglecting the contribution to the infidelity for  $s < s_c$ , we have

$$\mathcal{I} \simeq \epsilon^2 \left| e^{-i\alpha} \cdot \int_{t_1}^{t_2} dt V_{10}(s(t)) + \int_{t_3}^T dt V_{10}(s(t)) \right|^2, \quad (2)$$

where  $\alpha = \int_{t_2}^{t_3} d\tau \delta E(s(\tau))$ . By designing the protocol  $s(t)$  such that  $\alpha = \pi$  and  $\int_{t_1}^{t_2} dt V_{10} = \int_{t_3}^T dt V_{10}$ , these two amplitudes interfere destructively, thereby eliminating preparation infidelities at leading order in  $\epsilon$ . We call this protocol the *adiabatic echo protocol*, due to its analogy with spin echo sequences used in nuclear magnetic resonance and related contexts [26].

While the analytical argument above suggests that the echo protocol possesses a universal structure enhancing robustness against static perturbations, the precise control profile that realizes it depends on microscopic details such as critical point location, matrix elements, and energy gaps. In what follows, we consider concrete model Hamiltonians and use GRAPE to demonstrate the emergence of the echo protocol in the preparation of selected many-body target states.

*GHZ state preparation in the quantum Ising chain.* – We begin with the quantum Ising chain in transverse and longitudinal fields, targeting GHZ state preparation [27]. The Hamiltonian reads [28]:

$$\hat{H}_{\text{Ising}} = -J \sum_i \hat{\sigma}_i^z \hat{\sigma}_{i+1}^z - g \sum_i \hat{\sigma}_i^x + h \sum_i \hat{\sigma}_i^z, \quad (3)$$

where  $\hat{\sigma}_i^{x/z}$  are Pauli matrices. We parametrize the couplings  $J$  and  $g$  with a single control parameter  $s$  via  $J = \sin(\pi s/2)$  and  $g = \cos(\pi s/2)$ . For  $h = 0$ ,  $\hat{H}_{\text{Ising}}$  represents the unperturbed Hamiltonian  $\hat{H}_0$ , which has a  $\mathbb{Z}_2$  symmetry generated by  $\prod_i \hat{\sigma}_i^x$ . The critical point  $s_c = 1/2$  separates the disordered phase ( $s < s_c$ ) from the ordered one ( $s > s_c$ ). The last term in Eq. (3) breaks the symmetry and plays the role of the static perturbation  $\hat{V}$ .

The dynamical preparation is carried out by evolving the system under a time-dependent  $s(t)$ , starting from the product state  $|+\cdots+\rangle$ , i.e., the ground state of  $\hat{H}_0(s=0)$ . The target state is  $|\psi_{\text{GHZ}}^+\rangle = \frac{1}{\sqrt{2}}(|\uparrow\uparrow\cdots\uparrow\rangle + |\downarrow\downarrow\cdots\downarrow\rangle)$ , i.e., the ground state of  $\hat{H}_0(s=1)$ , exactly degenerate

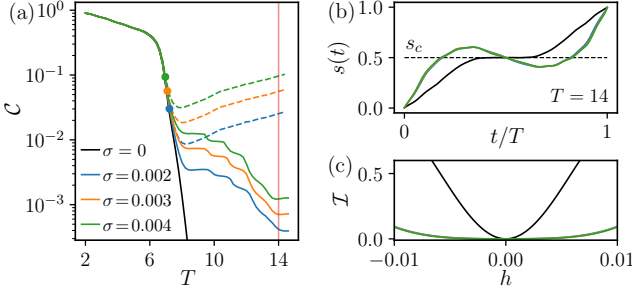


Figure 2. **Adiabatic echo in the quantum Ising chain.** (a) Optimal cost function Eq. (4) vs total preparation time, shown for various values of the maximal longitudinal field strength  $\sigma$ . For  $\sigma > 0$ , the optimization averages over  $N_s = 30$  samples. Dashed colored lines show the averaged infidelity when evaluated on the time-optimal protocols obtained for  $\sigma = 0$ . The colored dots in (a) indicate the point beyond which the optimization for  $\sigma > 0$  yields a solution that differs from the time-optimal one. (b) Optimized profiles  $s(t)$  for  $T = 14$  (vertical red line in (a)) and varying  $\sigma$ . The optimization for  $\sigma > 0$  takes the form of an echo protocol akin to the one sketched in Fig. 1b. (c) Preparation infidelity for the profiles in (b), plotted against the longitudinal field strength  $h$ .

with  $|\psi_{\text{GHZ}}^-\rangle = \frac{1}{\sqrt{2}}(|\uparrow\uparrow\cdots\uparrow\rangle - |\downarrow\downarrow\cdots\downarrow\rangle)$ . Both the initial and target states belong to the even  $\mathbb{Z}_2$  symmetry sector. The static field  $h$  couples these two sectors, inducing leakage from  $|\psi_{\text{GHZ}}^+\rangle$  to  $|\psi_{\text{GHZ}}^-\rangle$  when  $s(t) \gtrsim s_c$ , resulting in a loss of fidelity for the prepared GHZ state.

We apply GRAPE to optimize the control function  $s(t)$  for preparing  $|\psi_{\text{GHZ}}^+\rangle$ . The variational parameters are the values  $s_j = s(t_j)$  on a time grid of  $N$  points  $t_j = (j + \frac{1}{2})dt$ , where  $j = 0, \dots, N-1$ ,  $dt = T/N$ , and  $T$  is the total evolution time. We define the cost function as the preparation infidelity averaged over  $N_s$  values of the perturbation strength  $\epsilon_\ell$ :

$$\mathcal{C} = 1 - \frac{1}{N_s} \sum_{\ell=1}^{N_s} \left| \langle \psi_{\text{target}} | \prod_{j=0}^{N-1} e^{-idt[\hat{H}_0(s_j) + \epsilon_\ell \hat{V}]} | \psi_0 \rangle \right|^2, \quad (4)$$

where  $\epsilon$  is the longitudinal field  $h$  in Eq. (3), sampled uniformly in the interval  $[-\sigma, \sigma]$ . The case  $\sigma = 0$  ( $N_s = 1$ ) corresponds to the unperturbed control problem. The optimization is performed using standard routines that rely on the gradient  $\partial\mathcal{C}/\partial s_j$ , which can be efficiently computed numerically [25]. Moreover, to ensure the smoothness of the optimal control function, we add a term to  $\mathcal{C}$  that penalizes discontinuous solutions [25].

In Fig. 2a, we plot the optimal  $\mathcal{C}$  as a function of the preparation time  $T$  for various values of the maximal perturbation strength  $\sigma$ , for  $L = 18$  spins with periodic boundary conditions. The system-size scaling of these results is discussed in [25]. The solid black line represents purely time-optimal protocols obtained for  $\sigma = 0$ , while the dashed lines represent the corresponding averaged infidelities Eq. (4) evaluated for  $\sigma > 0$ . For small  $T$ , the

infidelity is dominated by non-adiabatic transitions within the even  $\mathbb{Z}_2$  sector, and the optimization for  $\sigma > 0$  leads to the same results as for  $\sigma = 0$ .

As  $T$  increases and the evolution turns adiabatic, the leakage to the odd  $\mathbb{Z}_2$  sector due to the perturbation becomes the main source of infidelity. In this regime, the optimal solution for  $\sigma > 0$  deviates from the  $\sigma = 0$  case and takes the form of the echo protocol discussed earlier. This is illustrated in Fig. 2b, where a typical time-optimal solution (black line), in which  $s(t)$  crosses  $s_c$  only once, is compared with an echo-like solution whose profile closely resembles Fig. 1b. Although the evolution time  $T$  at which the echo protocol becomes beneficial decreases as  $\sigma$  increases (cf. the colored markers in Fig. 2a), the control profile  $s(t)$  appears to be insensitive to the value of  $\sigma$ . In Fig. 2c, we plot the infidelity as a function of the longitudinal field  $h$  for the echo protocol (colored lines), demonstrating its significantly enhanced robustness compared to the time-optimal case (black line).

**GHZ state preparation in Rydberg atom arrays.** – As a second, experimentally relevant example, we turn to Rydberg atom arrays [29], a paradigmatic quantum platform that naturally features coherent control and strong interactions with static imperfections [30]. Each atom is modeled as a two-level system with ground state  $|g\rangle$  and Rydberg state  $|r\rangle$ , and the dynamics is described by the Hamiltonian

$$\hat{H}_{\text{Ryd}} = \sum_i \left( \frac{\Omega}{2} \hat{\sigma}_i^x - \Delta \hat{n}_i \right) + \sum_{i < j} U_{ij} \hat{n}_i \hat{n}_j, \quad (5)$$

where  $\hat{\sigma}_i^x = |g\rangle_i \langle r| + |r\rangle_i \langle g|$  and  $\hat{n}_i = |r\rangle_i \langle r|$ . Here,  $\Omega$  is the Rabi frequency,  $\Delta$  is the detuning, and  $U_{ij} \sim 1/|\mathbf{x}_i - \mathbf{x}_j|^6$  is the van der Waals interaction between atoms at positions  $\mathbf{x}_i$  and  $\mathbf{x}_j$ . The blockade radius  $R_b$  is defined as the characteristic length scale at which  $U_{R_b} = \Omega$ , marking the distance below which simultaneous Rydberg excitation is suppressed [31–33].

We consider arrays of 16 atoms on a square lattice [34, 35] and on a two-leg ladder [36–38] with open boundary conditions. Similarly to the Ising model,  $\hat{H}_{\text{Ryd}}$  possesses a  $\mathbb{Z}_2$  symmetry encoded as a lattice reflection exchanging the two sublattices, and, for a suitable choice of  $R_b$ , exhibits a disordered and an ordered phases, separated by a critical point. Below, we set  $R_b = 1.15a$ , where  $a$  is the lattice spacing.

We aim to prepare  $|\psi_{\text{GHZ}}^+\rangle = \frac{1}{\sqrt{2}}(|g\rangle_A |r\rangle_B + |r\rangle_A |g\rangle_B)$ , where  $|g\rangle_A |r\rangle_B$  denotes the configuration with all atoms in sublattice  $A$  ( $B$ ) in state  $|g\rangle$  ( $|r\rangle$ ), and vice versa. We initialize the system in the product state  $|\psi_0\rangle = |gg\cdots g\rangle$  and evolve it under the time-dependent Rydberg Hamiltonian in Eq. (5), with  $\Omega(t) = \Omega_0 w(t)$ , where  $w(t)$  is a window function satisfying  $w(0) = w(T) = 0$  [25]. We use the detuning  $\Delta(t)$  as the control function. Provided that  $\Delta(0) < 0$ ,  $\Delta(T) > 0$ , and the  $\mathbb{Z}_2$  symmetry is not explicitly broken,  $|\psi_0\rangle$  is the ground state for  $t = 0$ , while

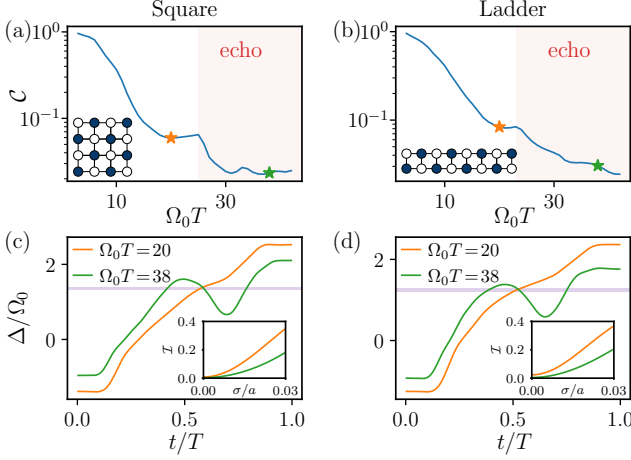


Figure 3. **GHZ state preparation in Rydberg arrays.** (a,b) Optimal cost function Eq. (4), on the square lattice (a) and on the ladder (b), vs total preparation time, for  $N_s = 30$  samples, each consisting of one displacement  $\delta \mathbf{x}_i$  per atom, gaussian distributed with standard deviation  $\sigma = 0.01a$ . In the shaded red region the optimal protocols acquire a profile typical of the echo mechanism. (c,d) Optimal control profiles on the square lattice (c) and on the ladder (d) for  $\Omega_0 T = 20$  (standard adiabatic) and  $\Omega_0 T = 38$  (adiabatic echo). The insets compare the robustness of the two against the standard deviation of the positional disorder. The shaded purple region marks the finite-size critical regime, estimated from two independent ground state diagnostics [25].

$|\psi_{\text{GHZ}}^+\rangle$  is the ground state for  $t \rightarrow T$ .

A relevant source of symmetry-breaking in this setting arises from static but spatially inhomogeneous atomic displacements, which vary from shot to shot and explicitly break the  $\mathbb{Z}_2$  lattice reflection symmetry (cf. Fig. 1d). These experimental imperfections are particularly significant due to the diagonal interaction  $U_{\sqrt{2}a} \simeq 0.3\Omega$ , which is comparable to the Rabi frequency.

To find robust GHZ preparation protocols, we apply GRAPE to the cost function Eq. (4), where each sample consists of one displacement  $\delta \mathbf{x}_i$  per atom, independently drawn from a gaussian distribution with zero mean and standard deviation  $\sigma = 0.01a$ . In Fig. 3, we show the optimization results for the square lattice (left) and ladder (right). As in the Ising model, the optimal control solution differs qualitatively from a standard adiabatic protocol beyond a characteristic time scale  $\Omega_0 T^* \simeq 20$  (colored region in Figs. 3a and 3b). The corresponding optimal profiles are shown in Figs. 3c and 3d: while for  $T < T^*$  the solution features a monotonic ramp-up of  $\Delta(t)$ , for  $T > T^*$  the optimal protocol exhibits the characteristic structure of the echo scheme, featuring three sweeps across the phase transition (cf. Fig. 3b). The insets of Figs. 3c and 3d highlight the robustness of the echo protocol, which was experimentally validated in a parallel study [24], enabling the preparation of GHZ states twice as large as those achievable with standard adiabatic protocols.

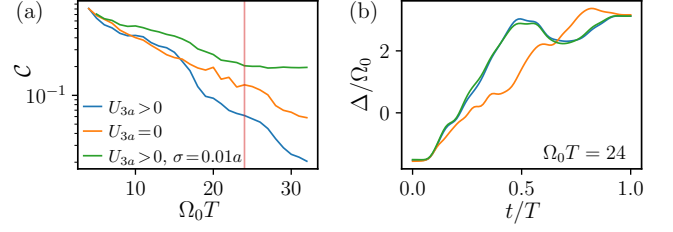


Figure 4. **RVB state preparation in Rydberg arrays.** (a) Optimal RVB preparation fidelity vs total preparation time on the ruby lattice with 24 atoms, truncating ( $U_{3a} = 0$ ) and including ( $U_{3a} > 0$ ) the van der Waals potential. For  $U_{3a} > 0$  the optimization is also performed including positional disorder via the cost function Eq. (4), averaged over  $N_s = 30$  gaussian distributed samples (green line). (b) Optimal control profiles for  $\Omega_0 T = 24$  (vertical red line in (a)). The optimal protocol exhibits the structure of the adiabatic echo only when  $U_{3a} > 0$ .

*Quantum spin liquid state preparation.* – As a final example, we consider Rydberg atoms on the ruby lattice and set  $R_b = 2.3a$  [39, 40]. Similarly to the GHZ preparation discussed above, we fix  $\Omega(t) = \Omega_0 w(t)$ , with  $w(0) = w(T) = 0$  [25], take  $\Delta(t)$  as the control function, with  $\Delta(0) < 0$  and  $\Delta(T) > 0$ , and initialize the system in the product state  $|gg \cdots g\rangle$ . For  $t = T$ , and with the van der Waals potential truncated as  $U_R = 0$  for  $R > \sqrt{7}a$ , the classical ground states correspond to all fully-packed dimer coverings of the kagome lattice [39]. Their equal-weight superposition—the resonating valence bond (RVB) state [41]—is a  $\mathbb{Z}_2$  quantum spin liquid [42], and is the target of our preparation. Previous works have demonstrated that this state can be prepared with high fidelity in this setting [43–45]. However, the inclusion of longer-range interaction tails  $U_{3a}$  lifts the degeneracy of the RVB components in the classical limit, imprinting relative phases during the evolution and thereby degrading the fidelity of the prepared state [43, 46].

While this perturbation does not explicitly break any microscopic symmetry of the Rydberg Hamiltonian on the ruby lattice, it plays a role analogous to the static perturbation  $\hat{V}$  in the GHZ preparation discussed earlier, with the two GHZ components replaced by exponentially many RVB configurations. To determine the optimal protocol for preparing the RVB state in this setting, we apply GRAPE to the full Hamiltonian Eq. (5) on a periodic cluster of 24 atoms, including all van der Waals interaction tails. Remarkably, as shown in Fig. 4b, the resulting optimal control profile displays the characteristic non-monotonic shape of the adiabatic echo. This solution is also robust, as the optimal protocol remains essentially unchanged when positional disorder is included in the optimization (cf. blue and green lines in Fig. 4b). In contrast, when the interaction is truncated at distance  $R = \sqrt{7}a$ , the optimal solution is monotonic (cf. orange line in Fig. 4b), confirming that the echo protocol arises

specifically to mitigate the effect of the long-range tails.

*Conclusions.* – We introduced the adiabatic echo protocol as a general approach to many-body quantum state preparation in the presence of static perturbations. Its key feature is the suppression of leading-order errors via dynamically engineered interference, which we analyzed both analytically and numerically. Going beyond standard approaches to many-body optimal control, which rely on restrictive parametrizations of the control fields [47, 48], we applied GRAPE to various interacting models and uncovered robust solutions that naturally exhibit the echo structure.

This work represents one of the first successful applications of unbiased optimal control methods to strongly interacting quantum systems, demonstrating their effectiveness in this complex setting. The adiabatic echo protocol introduced here offers a novel approach to robust quantum state preparation, with potential applicability across a wide range of platforms beyond those explicitly considered. Taken together, these findings open new directions for theoretical and numerical exploration of robust many-body quantum dynamics.

*Acknowledgments.* – We thank C. Fromenteil and P. Zoller for helpful discussions. This work is supported by the ERC Starting grant QARA (Grant No. 101041435), the Horizon Europe programme HORIZON-CL4-2022-QUANTUM02-SGA via the project 101113690 (PASQuanS2.1) and by the Austrian Science Fund (FWF) (Grant No. DOI 10.55776/COE1). G. G. acknowledges support from the European Union’s Horizon Europe program under the Marie Skłodowska Curie Action TOPORYD (Grant No. 101106005). A.B. acknowledges support by the Swiss National Science Foundation under grant No. 222216. A.M.K. acknowledges support by ONR (N00014-23-1-2533), AFOSR (FA9550-23-1-0097), and NIST.

---

\* These authors contributed equally to this work.

† [hannes.pichler@uibk.ac.at](mailto:hannes.pichler@uibk.ac.at)

- [1] M. A. Nielsen and I. L. Chuang, *Quantum Computation and Quantum Information*, 10th ed. (Cambridge University Press, 2000).
- [2] E. Farhi, J. Goldstone, S. Gutmann, and M. Sipser, Quantum computation by adiabatic evolution, *arXiv preprint arXiv:quant-ph/0001106* (2000).
- [3] R. Raussendorf and H. J. Briegel, A one-way quantum computer, *Physical Review Letters* **86**, 5188 (2001).
- [4] J. I. Cirac and P. Zoller, Goals and opportunities in quantum simulation, *Nature Physics* **8**, 264 (2012).
- [5] I. M. Georgescu, S. Ashhab, and F. Nori, Quantum simulation, *Rev. Mod. Phys.* **86**, 153 (2014).
- [6] C. Gross and I. Bloch, Quantum simulations with ultracold atoms in optical lattices, *Science* **357**, 995 (2017).
- [7] E. Altman, K. R. Brown, G. Carleo, L. D. Carr, E. Demler, C. Chin, B. DeMarco, S. E. Economou, M. A. Eriksson, K.-M. C. Fu, M. Greiner, K. R. Hazzard, R. G. Hulet, A. J. Kollár, B. L. Lev, M. D. Lukin, R. Ma, X. Mi, S. Misra, C. Monroe, K. Murch, Z. Nazario, K.-K. Ni, A. C. Potter, P. Roushan, M. Saffman, M. Schleier-Smith, I. Siddiqi, R. Simmonds, M. Singh, I. Spielman, K. Temme, D. S. Weiss, J. Vučković, V. Vuletić, J. Ye, and M. Zwierlein, Quantum Simulators: Architectures and Opportunities, *PRX Quantum* **2**, 017003 (2021).
- [8] V. Giovannetti, S. Lloyd, and L. Maccone, Advances in quantum metrology, *Nature Photonics* **5**, 222 (2011).
- [9] C. L. Degen, F. Reinhard, and P. Cappellaro, Quantum sensing, *Rev. Mod. Phys.* **89**, 035002 (2017).
- [10] J. Ye and P. Zoller, Essay: Quantum sensing with atomic, molecular, and optical platforms for fundamental physics, *Phys. Rev. Lett.* **132**, 190001 (2024).
- [11] J. Dziarmaga, Dynamics of a quantum phase transition and relaxation to a steady state, *Advances in Physics* **59**, 1063 (2010).
- [12] A. Polkovnikov, K. Sengupta, A. Silva, and M. Vengalattore, Colloquium: Nonequilibrium dynamics of closed interacting quantum systems, *Rev. Mod. Phys.* **83**, 863 (2011).
- [13] M. Kolodrubetz, D. Sels, P. Mehta, and A. Polkovnikov, Geometry and non-adiabatic response in quantum and classical systems, *Physics Reports* **697**, 1 (2017).
- [14] D. Sels and A. Polkovnikov, Minimizing irreversible losses in quantum systems by local counterdiabatic driving, *Proceedings of the National Academy of Sciences* **114**, E3909 (2017).
- [15] T. Albash and D. A. Lidar, Adiabatic quantum computation, *Rev. Mod. Phys.* **90**, 015002 (2018).
- [16] P. Hauke, F. M. Cucchietti, L. Tagliacozzo, I. Deutsch, and M. Lewenstein, Can one trust quantum simulators?, *Reports on Progress in Physics* **75**, 082401 (2012).
- [17] S. J. Glaser, U. Boscain, T. Calarco, C. P. Koch, W. Köckenberger, R. Kosloff, I. Kuprov, B. Luy, S. Schirmer, T. Schulte-Herbrüggen, D. Sugny, and F. K. Wilhelm, Training Schrödinger’s cat: quantum optimal control. Strategic report on current status, visions and goals for research in Europe, *European Physical Journal D* **69**, 279 (2015).
- [18] N. Khaneja, T. Reiss, C. Kehlet, T. Schulte-Herbrüggen, and S. J. Glaser, Optimal control of coupled spin dynamics: design of NMR pulse sequences by gradient ascent algorithms, *Journal of Magnetic Resonance* **172**, 296 (2005).
- [19] A. Garon, S. J. Glaser, and D. Sugny, Time-optimal control of SU(2) quantum operations, *Phys. Rev. A* **88**, 043422 (2013).
- [20] D. J. Egger and F. K. Wilhelm, Optimized controlled-Z gates for two superconducting qubits coupled through a resonator, *Superconductor Science and Technology* **27**, 014001 (2014).
- [21] F. Dolde, I. Jakobi, B. Naydenov, N. Zhao, S. Pezzagna, C. Trautmann, J. Meijer, P. Neumann, F. Jelezko, and J. Wrachtrup, High-fidelity spin entanglement using optimal control, *Nature Communications* **5**, 3371 (2014).
- [22] S. Jandura and G. Pupillo, Time-optimal two- and three-qubit gates for Rydberg atoms, *Quantum* **6**, 712 (2022).
- [23] G. Giudici, S. Veroni, G. Giudice, H. Pichler, and J. Zeiher, Fast entangling gates for Rydberg atoms via resonant dipole-dipole interaction, *arXiv preprint arXiv:2411.05073* (2024).

- [24] A. Senoo, A. Baumgärtner, J. W. Lis, G. M. Vaidya, Z. Zeng, G. Giudici, H. Pichler, and A. M. Kaufman, High-fidelity entanglement and coherent multi-qubit mapping in an atom array, [arXiv:2506.xxxxx](#) (2025).
- [25] See Supplemental Material.
- [26] E. L. Hahn, Spin echoes, *Phys. Rev.* **80**, 580 (1950).
- [27] X. Wang, A. Bayat, S. Bose, and S. Schirmer, Global control methods for GHZ state generation on 1-D Ising chain, *Physical Review A* **82**, 012330 (2010).
- [28] S. Suzuki, J.-i. Inoue, and B. K. Chakrabarti, *Quantum Ising Phases and Transitions in Transverse Ising Models*, Lecture Notes in Physics, Vol. 862 (Springer, Berlin, Heidelberg, 2013).
- [29] A. Browaeys and T. Lahaye, Many-body physics with individually controlled Rydberg atoms, *Nature Physics* **16**, 132 (2020).
- [30] J. Wurtz, A. Bylinskii, B. Braverman, J. Amato-Grill, S. H. Cantu, F. Huber, A. Lukin, F. Liu, P. Weinberg, J. Long, S.-T. Wang, N. Gemelke, and A. Keesling, Aquila: QuEra's 256-qubit neutral-atom quantum computer, [arXiv preprint arXiv:2306.11727](#) (2023).
- [31] D. Jaksch, J. I. Cirac, P. Zoller, S. L. Rolston, R. Côté, and M. D. Lukin, Fast quantum gates for neutral atoms, *Phys. Rev. Lett.* **85**, 2208 (2000).
- [32] M. D. Lukin, M. Fleischhauer, R. Cote, L. M. Duan, D. Jaksch, J. I. Cirac, and P. Zoller, Dipole blockade and quantum information processing in mesoscopic atomic ensembles, *Phys. Rev. Lett.* **87**, 037901 (2001).
- [33] A. Gaëtan, Y. Miroshnychenko, T. Wilk, A. Chotia, M. Viteau, D. Comparat, P. Pillet, A. Browaeys, and P. Grangier, Observation of collective excitation of two individual atoms in the Rydberg blockade regime, *Nature Physics* **5**, 115 (2009).
- [34] R. Samajdar, W. W. Ho, H. Pichler, M. D. Lukin, and S. Sachdev, Complex density wave orders and quantum phase transitions in a model of square-lattice Rydberg atom arrays, *Phys. Rev. Lett.* **124**, 103601 (2020).
- [35] S. Ebadi, T. T. Wang, H. Levine, A. Keesling, G. Semeghini, A. Omran, D. Bluvstein, R. Samajdar, H. Pichler, W. W. Ho, S. Choi, S. Sachdev, M. Greiner, V. Vuletić, and M. D. Lukin, Quantum phases of matter on a 256-atom programmable quantum simulator, *Nature* **595**, 227–232 (2021).
- [36] L. Eck and P. Fendley, Critical lines and ordered phases in a Rydberg-blockade ladder, *Physical Review B* **108**, 125135 (2023).
- [37] J. Soto-Garcia and N. Chepiga, Numerical investigation of quantum phases and phase transitions in a two-leg ladder of Rydberg atoms, *Phys. Rev. Research* **7**, 013215 (2025).
- [38] J. Zhang, S. H. Cantú, F. Liu, A. Bylinskii, B. Braverman, F. Huber, J. Amato-Grill, A. Lukin, N. Gemelke, A. Keesling, S.-T. Wang, Y. Meurice, and S.-W. Tsai, Probing quantum floating phases in Rydberg atom arrays, *Nature Communications* **16**, 712 (2025).
- [39] R. Verresen, M. D. Lukin, and A. Vishwanath, Prediction of Toric Code topological order from Rydberg blockade, *Phys. Rev. X* **11**, 031005 (2021).
- [40] G. Semeghini, H. Levine, A. Keesling, S. Ebadi, T. T. Wang, D. Bluvstein, R. Verresen, H. Pichler, M. Kalinowski, R. Samajdar, A. Omran, S. Sachdev, A. Vishwanath, M. Greiner, V. Vuletić, and M. D. Lukin, Probing topological spin liquids on a programmable quantum simulator, *Science* **374**, 1242 (2021).
- [41] P. W. Anderson, Resonating valence bonds: A new kind of insulator?, *Materials Research Bulletin* **8**, 153 (1973).
- [42] R. Moessner and K. S. Raman, Quantum dimer models, in *Introduction to Frustrated Magnetism*, edited by C. Lacroix, P. Mendels, and F. Mila (Springer, 2011) pp. 437–479.
- [43] G. Giudici, M. D. Lukin, and H. Pichler, Dynamical preparation of quantum spin liquids in Rydberg atom arrays, *Physical Review Letters* **129**, 090401 (2022).
- [44] R. Sahay, A. Vishwanath, and R. Verresen, Quantum spin puddles and lakes: NISQ-Era spin liquids from non-equilibrium dynamics, [arXiv preprint arXiv:2211.01381](#) (2022).
- [45] N. O. Gjonbalaj, R. Sahay, and S. F. Yelin, Shortcuts to analog preparation of non-equilibrium quantum lakes, [arXiv preprint arXiv:2502.03518](#) (2025).
- [46] Z. Zeng, G. Giudici, and H. Pichler, Quantum dimer models with Rydberg gadgets, *Phys. Rev. Research* **7**, L012006 (2025).
- [47] T. Caneva, T. Calarco, and S. Montangero, Chopped random-basis quantum optimization, *Phys. Rev. A* **84**, 022326 (2011).
- [48] A. Omran, H. Levine, A. Keesling, G. Semeghini, T. T. Wang, S. Ebadi, H. Bernien, A. S. Zibrov, H. Pichler, S. Choi, J. Cui, M. Rossignolo, P. Rembold, S. Montangero, T. Calarco, M. Endres, M. Greiner, V. Vuletić, and M. D. Lukin, Generation and manipulation of Schrödinger cat states in Rydberg atom arrays, *Science* **365**, 570 (2019).
- [49] A. H. Al-Mohy and N. J. Higham, Computing the Fréchet derivative of the matrix exponential, with an application to condition number estimation, *SIAM Journal on Matrix Analysis and Applications* **30**, 1639 (2009).
- [50] J. Haegeman, C. Lubich, I. Oseledets, B. Vandereycken, and F. Verstraete, Unifying time evolution and optimization with matrix product states, *Phys. Rev. B* **94**, 165116 (2016).
- [51] P. Virtanen, R. Gommers, T. E. Oliphant, M. Haberland, T. Reddy, D. Cournapeau, E. Burovski, P. Peterson, W. Weckesser, J. Bright, S. J. van der Walt, M. Brett, J. Wilson, K. J. Millman, N. Mayorov, A. R. J. Nelson, E. Jones, R. Kern, E. Larson, C. J. Carey, *et al.*, SciPy 1.0: Fundamental Algorithms for Scientific Computing in Python, *Nature Methods* **17**, 261 (2020).
- [52] P. Zanardi and N. Paunković, Ground state overlap and quantum phase transitions, *Phys. Rev. E* **74**, 031123 (2006).
- [53] S.-J. Gu, Fidelity approach to quantum phase transitions, *International Journal of Modern Physics B* **24**, 4371 (2010).
- [54] H. Bernien, S. Schwartz, A. Keesling, H. Levine, A. Omran, H. Pichler, S. Choi, A. S. Zibrov, M. Endres, M. Greiner, V. Vuletić, and M. D. Lukin, Probing many-body dynamics on a 51-atom quantum simulator, *Nature* **551**, 579–584 (2017).

# Supplementary Material

## Contents

I. Preparation infidelity from time-dependent perturbation theory	7
II. Contribution to the preparation infidelity from the trivial phase	8
III. Optimal control via GRAPE	9
IV. Finite-size scaling of the GHZ state preparation in the quantum Ising chain	10
V. Phase transition location in Rydberg atom arrays	11
VI. Adiabatic echo protocol with $\mathbb{Z}_3$ and $\mathbb{Z}_4$ symmetry breaking	11

### I. Preparation infidelity from time-dependent perturbation theory

In this section we derive the expression for the preparation infidelity used in the main text. We consider the time-dependent Hamiltonian  $\hat{H}(s(t)) = \hat{H}_0(s(t)) + \epsilon \hat{V}$ . We want to prepare the ground state of  $\hat{H}_0(s(T))$ , i.e.,  $|\psi_{\text{target}}\rangle = |E_0(s(T))\rangle$ , starting from the ground state  $|E_0(s(0))\rangle$  of  $\hat{H}_0(s(0))$ . To lighten notation, we drop the explicit dependence on the control parameter  $s$ . The preparation infidelity is defined as

$$\mathcal{I} = 1 - |\langle \psi_{\text{target}} | \psi(T) \rangle|^2 = 1 - \left| \langle E_0(T) | \hat{U}(T) | E_0(0) \rangle \right|^2 = \sum_{n \neq 0} \left| \langle E_n(T) | \hat{U}(T) | E_0(0) \rangle \right|^2, \quad (\text{S1})$$

where in the last step we used the completeness of the eigenbasis  $\{|E_n(T)\rangle\}$ .

In the interaction picture, the full time-evolution operator decomposes as  $\hat{U}(T) = \hat{U}_0(T) \hat{U}_I(T)$ , where:

$$\hat{U}_I(T) = \exp \left( -i\epsilon \int_0^T dt \hat{U}_0^\dagger(t) \hat{V} \hat{U}_0(t) \right) \simeq 1 - i\epsilon \int_0^T dt \hat{U}_0^\dagger(t) \hat{V} \hat{U}_0(t). \quad (\text{S2})$$

Assuming adiabatic evolution, we approximate the unperturbed dynamics as

$$\hat{U}_0(t) |E_n(0)\rangle \simeq \exp \left( -i \int_0^t d\tau E_n(\tau) + i \int_0^t d\tau \langle E_n(\tau) | \partial_\tau E_n(\tau) \rangle \right) |E_n(t)\rangle =: e^{i\phi_n(t)} |E_n(t)\rangle, \quad (\text{S3})$$

such that Eq. (S1) becomes:

$$\mathcal{I} = \sum_{n \neq 0} \left| \langle E_n(T) | \hat{U}_0(T) \hat{U}_I(T) | E_0(0) \rangle \right|^2 \simeq \sum_{n \neq 0} \left| e^{i\phi_n(T)} \langle E_n(0) | \hat{U}_I(T) | E_0(0) \rangle \right|^2 \simeq \quad (\text{S4})$$

$$\simeq \epsilon^2 \sum_{n \neq 0} \left| \int_0^T dt \langle E_n(0) | \hat{U}_0^\dagger(t) \hat{V} \hat{U}_0(t) | E_0(0) \rangle \right|^2 = \epsilon^2 \sum_{n \neq 0} \left| \int_0^T dt \langle E_n(t) | \hat{V} | E_0(t) \rangle e^{-i(\phi_n(t) - \phi_0(t))} \right|^2. \quad (\text{S5})$$

We now observe that the infidelity  $\mathcal{I}$  is invariant under local phase redefinitions of the instantaneous eigenstates  $\{|E_n(t)\rangle\}$ . We exploit this freedom by choosing a gauge in which the Berry connection vanishes along the preparation path:  $\langle E_n(\tau) | \partial_\tau E_n(\tau) \rangle = 0$ . Using the identity  $\int_0^t d\tau E_n(\tau) = \int_0^T d\tau E_n(\tau) - \int_t^T d\tau E_n(\tau)$ , and retaining only the dominant contribution from the first excited state, the preparation infidelity at leading order becomes:

$$\mathcal{I} \simeq \epsilon^2 \left| \int_0^T dt \langle E_1(t) | \hat{V} | E_0(t) \rangle e^{-i \int_t^T d\tau (E_1(\tau) - E_0(\tau))} \right|^2. \quad (\text{S6})$$

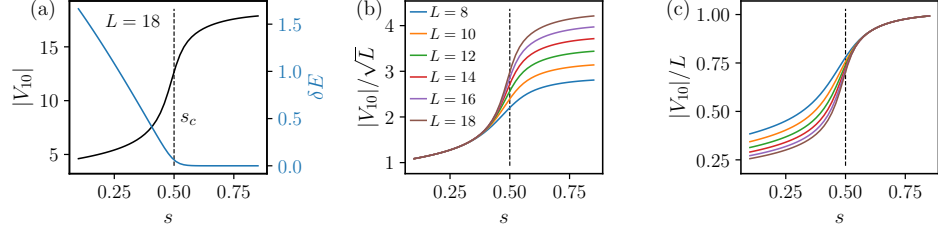


Figure S1. (a) Symmetry-breaking matrix element  $|V_{10}|$  (black) and lowest energy gap  $\delta E$  (blue) as functions of the control parameter  $s$  (cf. Eq. (3) of the main text and discussion below) for  $L = 18$ . The vertical line marks the critical point  $s_c = 1/2$ . (b,c) Rescaling  $|V_{10}|$  by  $\sqrt{L}$  (b) and  $L$  (c) results in curve collapse for  $s < s_c$  and  $s > s_c$ , respectively, demonstrating  $V_{10}(s < s_c) \sim \sqrt{L}$  and  $V_{10}(s > s_c) \sim L$ .

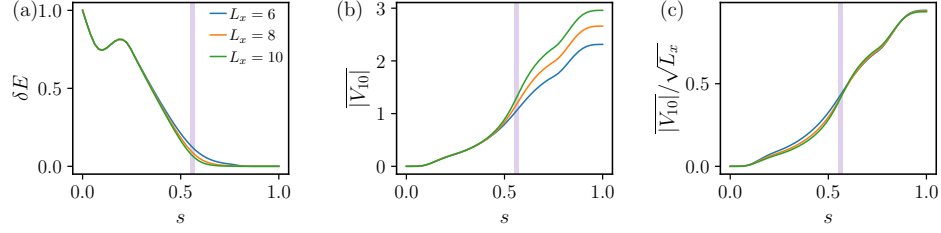


Figure S2. (a) Lowest energy gap  $\delta E$  as a function of the control parameter  $s$  for the Rydberg Hamiltonian on a ladder (cf. Eq (5) of the main text) with  $\Omega(s) = \Omega_0 w(s)$  (cf. Fig. S3) and  $\Delta(s) = \Omega_0(-1 + 4s)$ , for various ladder lengths  $L_x$ . The vertical shaded region marks the phase transition regime discussed in Section V. (b,c) Curve collapse of the symmetry-breaking matrix element  $\overline{V_{10}}(s)$ , averaged over 1000 realizations of the positional disorder. For  $s < s_c$ ,  $\overline{V_{10}}(s)$  is independent of  $L_x$  (b), while for  $s > s_c$  the data collapse shows  $\overline{V_{10}}(s) \sim \sqrt{L_x}$  (c).

## II. Contribution to the preparation infidelity from the trivial phase

In the main text, we neglected the contribution to the preparation infidelity coming from regions where the control field  $s(t)$  lies in the disordered phase of the Hamiltonian  $\hat{H}(s)$ , i.e.,  $s < s_c$ . To justify this approximation, we divide the protocol into segments separated by crossings of the critical point  $s_c$ , so that within each segment, either  $s(t) < s_c$  or  $s(t) > s_c$  holds throughout. We label the segments by  $k$ , and approximate  $V_{10}(s) \simeq V_{10}^k$  and  $\delta E(s) \simeq \delta E_k$  within each one. From Eq. (1) of the main text, the infidelity becomes

$$\mathcal{I} \simeq \epsilon^2 \left| \sum_k e^{i\alpha_k} V_{10}^k \frac{e^{i\delta E_k T_k} - 1}{\delta E_k} \right|^2 = \epsilon^2 \left| \sum_k A_k \right|^2, \quad (\text{S7})$$

where  $T_k$  is the time spent in interval  $k$  and  $\alpha_k$  is the dynamical phase accumulated before interval  $k$ .

In the trivial phase ( $s < s_c$ ),  $\delta E_k$  is finite, so  $A_k \sim e^{i\alpha_k} V_{10}^k / \delta E_k$ . In the ordered phase ( $s > s_c$ ), by contrast, the gap  $\delta E_k$  is exponentially small in the system size  $L$ , such that  $\delta E_k T_k \ll 1$ , yielding  $A_k \simeq e^{i\alpha_k} V_{10}^k T_k$ . Since adiabaticity requires  $T_k \sim L$ , we have  $A_k(s > s_c) \sim V_{10}^k L$ , while  $A_k(s < s_c) \sim V_{10}^k$ . Moreover, as we show below in two explicit examples, the matrix element  $V_{10}(s < s_c)$  is parametrically suppressed with system size compared to  $V_{10}(s > s_c)$ .

In the Ising model,  $\hat{V} = \sum_i \hat{\sigma}_i^z$ , and the system-size scaling of  $V_{10}$  can be computed analytically for both  $s = 0$  and  $s = 1$ . For  $s = 0$ , corresponding to the disordered phase, the ground state is  $|E_0\rangle = |+\dots+\rangle$  and the first excited state is  $|E_1\rangle = \frac{1}{\sqrt{L}} \sum_i \hat{\sigma}_i^z |E_0\rangle$ , yielding  $\langle E_1 | \hat{V} | E_0 \rangle = \sqrt{L}$ . For  $s = 1$ , deep in the ordered phase, the ground and first excited states are  $|E_0\rangle = \frac{1}{\sqrt{2}}(|\uparrow\uparrow\dots\uparrow\rangle + |\downarrow\downarrow\dots\downarrow\rangle)$  and  $|E_1\rangle = \frac{1}{\sqrt{2}}(|\uparrow\uparrow\dots\uparrow\rangle - |\downarrow\downarrow\dots\downarrow\rangle)$ , respectively, leading to  $\langle E_1 | \hat{V} | E_0 \rangle = L$ . As shown in Fig. S1, these distinct scaling behaviors persist throughout their respective phases, leading to additional system-size suppression of the amplitude  $A_k$  in the disordered regime:  $A_k(s < s_c) / A_k(s > s_c) \sim 1/L^{3/2}$ .

We observe the same scaling behavior in Rydberg atom arrays. In this case, the symmetry-breaking perturbation takes the form

$$\hat{V} = \frac{a}{\sigma} \Omega_0 \sum_{i < j} \left( \frac{R_b^6}{|(\mathbf{x}_i + \delta \mathbf{x}_i) - (\mathbf{x}_j + \delta \mathbf{x}_j)|^6} - \frac{R_b^6}{|\mathbf{x}_i - \mathbf{x}_j|^6} \right), \quad (\text{S8})$$

where  $\delta \mathbf{x}_i$  is a gaussian-distributed displacement with zero mean and standard deviation  $\sigma$ , and the prefactor is chosen so that  $\hat{V}$  is independent of  $\sigma/a$  for  $\sigma/a \ll 1$ . We focus on the ladder geometry and evaluate  $|V_{10}(s)|$  for the Rydberg Hamiltonian (Eq. (5) of the main text), averaging over 1000 disorder realizations. Here  $0 \leq s \leq 1$ , with  $\Omega(s) = \Omega_0 w(s)$  (see Fig. S3) and  $\Delta(s) = \Omega_0(-1 + 4s)$ . The resulting  $\overline{V_{10}(s)}$  is shown in Fig. S2, where the overline denotes the disorder average. We find  $\overline{V_{10}(s)} \sim \text{const}$  for  $s < s_c$ , while  $\overline{V_{10}(s)} \sim \sqrt{L_x}$  for  $s > s_c$ , where  $L_x$  is the linear size of the ladder. As in the Ising case, this implies  $A_k(s < s_c)/A_k(s > s_c) \sim 1/L_x^{3/2}$ .

### III. Optimal control via GRAPE

In this section, we review the optimal control methods used to optimize the profile of the control parameter  $s(t)$ . The cost function is defined as the infidelity between the prepared state and the target state:

$$\mathcal{C} = 1 - |\langle \psi_{\text{target}} | \hat{U}(T) | \psi_0 \rangle|^2 \simeq 1 - |\langle \psi_{\text{target}} | \prod_{j=0}^{N-1} \hat{U}_j | \psi_0 \rangle|^2, \quad (\text{S9})$$

where the time-evolution operator is discretized into  $N$  steps with  $dt = T/N$ , such that  $\hat{U}_j = \exp(-i\hat{H}(s_j)dt)$ ,  $s_j = s(t_j)$ , and  $t_j = (j + \frac{1}{2})dt$ , where  $j = 0, \dots, N-1$ . In this work, we used  $N = 150$ . We employ a gradient descent algorithm to minimize  $\mathcal{C}$ . The gradient of the cost function with respect to the control parameter  $s_i$  at each time is

$$\frac{\partial \mathcal{C}}{\partial s_i} = 2\text{Re} \left( \langle \psi(T) | \psi_{\text{target}} \rangle \langle \psi_{\text{target}} | \left( \prod_{k=j+1}^{N-1} \hat{U}_k \right) \frac{d\hat{U}_j}{ds_j} \left( \prod_{k=0}^{j-1} \hat{U}_k \right) | \psi_0 \rangle \right). \quad (\text{S10})$$

The derivative  $\frac{d\hat{U}_j}{ds_j}$  has to be treated with care when  $\hat{H}(s_j)$  and  $\frac{d\hat{H}(s_j)}{ds_j}$  do not commute. One has

$$\frac{d\hat{U}_j}{ds_j} = \lim_{h \rightarrow 0} \frac{\exp(-idt\hat{H}(s_j + h)) - \exp(-idt\hat{H}(s_j))}{h} = \lim_{h \rightarrow 0} \frac{\exp(-idt(\hat{H}(s_j) + h\frac{d\hat{H}(s_j)}{ds_j})) - \exp(-idt\hat{H}(s_j))}{h}. \quad (\text{S11})$$

For an exact numerical evaluation of the r.h.s. one can use the formula [49]

$$f \left( \begin{bmatrix} X & E \\ 0 & X \end{bmatrix} \right) = \begin{bmatrix} f(X) & Df(X, E) \\ 0 & f(X) \end{bmatrix}, \quad \text{where} \quad Df(X, E) = \lim_{h \rightarrow 0} \frac{f(X + hE) - f(X)}{h}, \quad (\text{S12})$$

with  $f = \exp$ ,  $X = -idt\hat{H}(s_j)$ , and  $E = -idt\frac{d\hat{H}(s_j)}{ds_j}$ . Eq. (S12) is amenable to efficient computation via Krylov-based algorithms for sparse matrices or tensor network methods based on the time-dependent variational principle (TDVP) [50]. In practice, for the time-steps and system sizes considered in this work, we employed the simple approximation

$$\frac{d\hat{U}_j}{ds_j} \simeq -idt \frac{d\hat{H}(s_j)}{ds_j} \hat{U}_j, \quad (\text{S13})$$

which can be straightforwardly computed with sparse matrix routines.

For the gradient-descent minimization, we used the L-BFGS-B algorithm from the SciPy package [51]. The optimization is performed iteratively, beginning with a short total evolution time  $T$  and a linear profile as the initial guess. Upon convergence, we increase  $T$  as  $T = T + dT$  and use the previously optimized profile as the initial guess.

In practical implementations, the control function  $s(t)$  must vary smoothly to ensure experimental feasibility. To enforce this, we add a regularization term to the cost function that penalizes rapid variations of  $s(t)$  [18]:

$$\mathcal{C}_\eta = \mathcal{C} + \eta \int_0^1 du \left( \frac{ds}{du} \right)^2 \simeq \mathcal{C} + \eta N \sum_i (s(t_{i+1}) - s(t_i))^2, \quad (\text{S14})$$

where  $u = t/T$  is the rescaled time and  $\eta$  is the strength of the regularization. Throughout this work, we fix  $\eta = 10^{-3}$ . Additionally, one can impose boundary conditions  $s(0) = s_0$  and  $s(T) = s_f$  by adding a penalty term that fixes the initial and final values:

$$\mathcal{C}_{\eta,\mu} = \mathcal{C}_\eta + \mu ((s(0) - s_0)^2 + (s(T) - s_f)^2), \quad (\text{S15})$$

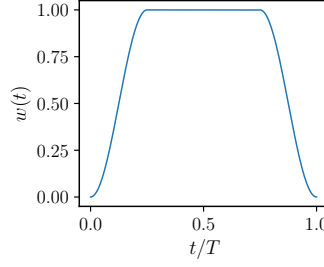


Figure S3. Cosine-tapered window function Eq. (S16) with  $\alpha = 0.25$ .

for some constant  $\mu \gg \mathcal{C}_0$ . In this work, we enforce boundary conditions  $s(0) = 0$  and  $s(T) = 1$  for the GHZ state preparation in the ferromagnetic quantum Ising chain, by setting  $\mu = 1$ .

The discussion above extends by linearity to the evaluation of the gradient of the cost function in Eq. (4) of the main text.

For the Rydberg array preparation of GHZ and RVB states (cf. Fig. 3 and Fig. 4 of the main text), we take the detuning  $\Delta(t)$  as the control function and parameterize the Rabi frequency as  $\Omega(t) = \Omega_0 w(t)$ , where  $w(t)$  is a cosine-tapered window of total duration  $T$  (cf. Fig. S3):

$$w(t) = \begin{cases} \frac{1}{2} \left[ 1 + \cos\left(\frac{\pi t}{\alpha T}\right) \right], & 0 \leq t < \alpha T \\ 1, & \alpha T \leq t \leq \frac{T}{2} \\ w(T - t), & \frac{T}{2} < t \end{cases} \quad (\text{S16})$$

Here, the parameter  $\alpha$  sets the rise (and fall) time relative to the total preparation time. We use  $\alpha = 0.25$  for the GHZ preparation and  $\alpha = 0.15$  for the RVB preparation, chosen to minimize the infidelity in the regime  $\Omega_0 T \lesssim 35$ .

In principle, the Rabi frequency  $\Omega(t)$  could also be treated as an independent control function. However, we find that doing so significantly slows convergence due to a more complex optimization landscape, while yielding only marginal improvements in fidelity.

#### IV. Finite-size scaling of the GHZ state preparation in the quantum Ising chain

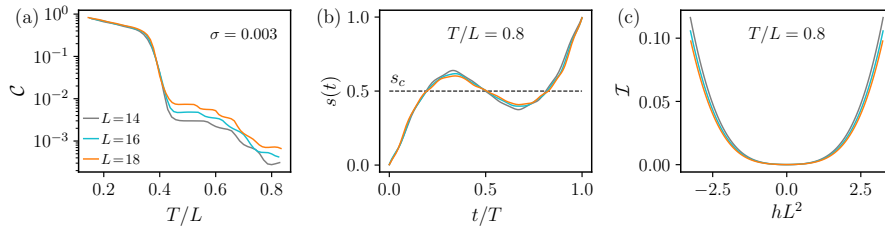


Figure S4. (a) Optimal cost function vs total preparation time  $T$  for various system sizes  $L$ . The optimization is performed via the cost function Eq. (4) of the main text, averaged over  $N_s = 30$  samples. (b) Optimized control profiles  $s(t)$  for fixed  $T/L = 0.8$  while varying  $L$ . (c) Corresponding preparation infidelity for the control protocols in (b), plotted against the scaled longitudinal field strength  $hL^2$ .

In the main text, we applied GRAPE optimization to the cost function in Eq. (4) to prepare the GHZ state in a quantum Ising chain of length  $L = 18$ , subject to a symmetry-breaking longitudinal field  $h$ . Here, we present a finite-size scaling analysis of those results, considering system sizes  $L = 14, 16, 18$ . Figure S4a shows the optimized cost function  $\mathcal{C}$  (Eq. (4) in the main text), averaged over  $N_s = 30$  perturbation samples, as a function of the total preparation time  $T$ . We observe a collapse of the curves when plotted against  $T/L$ , a hallmark of adiabatic protocols. In Fig. S4b, we show that the optimal control profile  $s(t)$  is essentially independent of  $L$  when plotted at fixed  $T/L$ .

Finally, Fig. S4c displays the preparation infidelity  $\mathcal{I}$  as a function of the rescaled perturbation strength  $hL^2$ . The approximate data collapse can be understood from the first-order expression of the infidelity in Eq. (S6). As discussed

in the main text, the dominant contribution to  $\mathcal{I}$  arises from the ordered phase, where  $V_{10} \sim L$ . Since  $T \sim L$ , one obtains  $\mathcal{I}(h, L) \simeq h^2 T^2 (V_{10})^2 \sim h^2 L^4 = (hL^2)^2$ . The validity of this scaling confirms that the echo protocol does not exactly cancel the first-order error due to the perturbation, while significantly suppressing its prefactor (cf. Fig. 2c of the main text).

### V. Phase transition location in Rydberg atom arrays

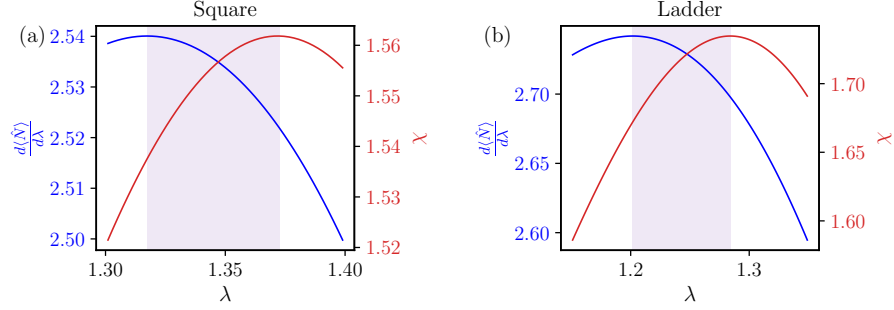


Figure S5. Finite-size critical regime for arrays of 16 Rydberg atoms with  $R_b = 1.15a$  on (a) a square lattice ( $4 \times 4$ ) and (b) a ladder ( $8 \times 2$ ). The shaded purple region marks the finite-size critical regime, and it is bounded by the peak of the excitation-number derivative (blue) and the peak of the fidelity susceptibility (red).

In the main text, we made use of the finite-size location of the transition point for Rydberg atoms on the square lattice and on the ladder. In Fig. 3c and Fig. 3d, we drew the critical regime as a purple horizontal narrow region, which we define as the interval between the transition points identified by two ground state diagnostics: (i) the derivative of the excitation number

$$\frac{d}{d\lambda} \langle E_0(\lambda) | \hat{N} | E_0(\lambda) \rangle \simeq \frac{\langle E_0(\lambda + \delta\lambda) | \hat{N} | E_0(\lambda + \delta\lambda) \rangle - \langle E_0(\lambda) | \hat{N} | E_0(\lambda) \rangle}{\delta\lambda}, \quad (\text{S17})$$

and (ii) the ground-state fidelity susceptibility [52, 53]

$$\chi = -\frac{2}{\delta\lambda^2} \ln |\langle E_0(\lambda) | E_0(\lambda + \delta\lambda) \rangle|, \quad (\text{S18})$$

where  $\lambda = \Delta/\Omega$ ,  $|E_0(\lambda)\rangle$  is the ground state wavefunction, and  $\delta\lambda$  a small variation in  $\lambda$ . The peaks of these two quantities serve as approximate indicators of criticality.

In Fig. S5, we show the critical regimes for 16 atoms on a square lattice ( $4 \times 4$ ) and on a ladder ( $8 \times 2$ ), where we used  $\delta\lambda = 0.002$ .

### VI. Adiabatic echo protocol with $\mathbb{Z}_3$ and $\mathbb{Z}_4$ symmetry breaking

In the main text, we presented an analytical argument explaining the robustness of the echo protocol in the presence of  $\mathbb{Z}_2$  symmetry breaking, based on the first-order expression for the preparation infidelity given in Eq. (S6). For systems with  $\mathbb{Z}_n$  symmetry, this expression generalizes to

$$\mathcal{I} \simeq \epsilon^2 \sum_{k=1}^{n-1} \left| \int_0^T dt V_{k0}(s(t)) e^{-i \int_t^T d\tau \delta E_k(s(\tau))} \right|^2, \quad (\text{S19})$$

where  $V_{k0}(s) = \langle E_k(s) | \hat{V} | E_0(s) \rangle$  and  $\delta E_k(s) = E_k(s) - E_0(s)$  are, respectively, the matrix elements and energy gaps between the ground state  $|E_0(s)\rangle$  and the first  $n-1$  excited states  $|E_k(s)\rangle$ . We assume that  $|E_0(s)\rangle$  is even under  $\mathbb{Z}_n$ , while each of the excited states  $|E_k(s)\rangle$  carries a distinct nontrivial  $\mathbb{Z}_n$  charge  $k = 1, \dots, n-1$ . In the ordered phase, where the  $\mathbb{Z}_n$  symmetry is spontaneously broken, the corresponding energy gaps  $\delta E_k$  become exponentially small in the system size.

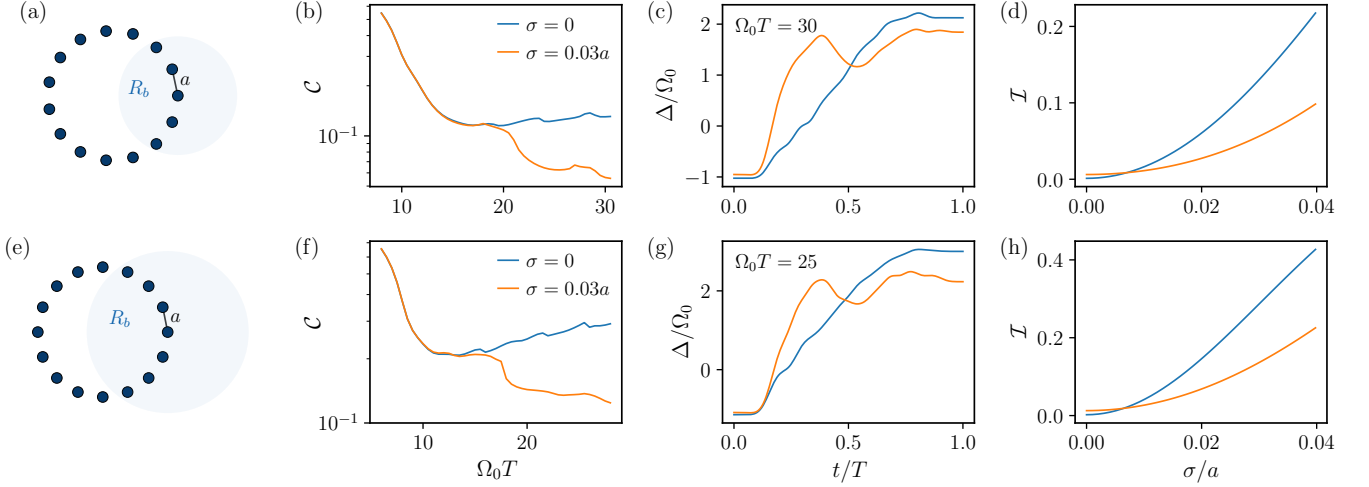


Figure S6. (a,e)  $L$  Rydberg atoms on a ring with blockade radius  $R_b$ : (a)  $L = 15$  and  $R_b = 2.2a$  for  $\mathbb{Z}_3$  symmetry breaking; (e)  $L = 16$  and  $R_b = 3a$  for  $\mathbb{Z}_4$  symmetry breaking. (b, f) Optimal cost function in the presence of positional disorder with  $\sigma = 0.03a$  vs total evolution time  $\Omega_0 T$ . The GRAPE optimization is performed with  $\sigma = 0$  (blue line) and  $\sigma = 0.03a$  (orange line). (c, g) Optimal profile for  $\Omega_0 T = 30$  for  $\mathbb{Z}_3$  (c) and  $\Omega_0 T = 25$  for  $\mathbb{Z}_4$  (g). Blue and orange lines correspond to the optimal protocols found for  $\sigma = 0$  (standard adiabatic) and  $\sigma = 0.03a$  (adiabatic echo), respectively. (d, h) Preparation infidelity as a function of the disorder strength  $\sigma$  for the protocols shown in (c,g).

Applying the same reasoning as in the  $\mathbb{Z}_2$  case to an echo protocol with turning points at  $t_1$ ,  $t_2$ , and  $t_3$ , we obtain

$$\mathcal{I} \simeq \epsilon^2 \sum_{k=1}^{n-1} \left| e^{-i\alpha_k} \cdot \int_{t_1}^{t_2} dt V_{k0}(s(t)) + \int_{t_3}^T dt V_{k0}(s(t)) \right|^2, \quad (\text{S20})$$

where  $\alpha_k = \int_{t_2}^{t_3} d\tau \delta E_k(s(\tau))$ . For the first-order contributions to cancel, each term in the sum must vanish individually. In general, this is not guaranteed unless both  $\delta E_k$  and  $V_{k0}(s)$  are independent of the  $\mathbb{Z}_n$  charge label  $k$ . When this condition holds, the argument for destructive interference leading to suppression of infidelity extends directly from  $\mathbb{Z}_2$  to  $\mathbb{Z}_n$ , and the emergence of the echo protocol is similarly justified. Below, we show that, consistent with this expectation, the echo structure arises in two concrete models exhibiting  $\mathbb{Z}_3$  and  $\mathbb{Z}_4$  symmetry breaking.

We consider Rydberg atoms arranged in a ring geometry, governed by the Hamiltonian in Eq. (5) of the main text, and study two different blockade radii:  $R_b = 2.2a$  and  $R_b = 3a$ . As in the square lattice and two-leg ladder setups discussed previously, a  $\mathbb{Z}_n$  symmetry emerges from the  $\mathbb{Z}_L$  translational symmetry of the ring, provided that the number of atoms  $L$  is a multiple of  $n$  (cf. Figs. S6a and S6e). In particular, for  $R_b = 2.2a$  with  $L$  a multiple of 3, and  $R_b = 3a$  with  $L$  a multiple of 4, the  $\mathbb{Z}_3$  and  $\mathbb{Z}_4$  translation symmetries are spontaneously broken at large enough detuning  $\Delta$  [54]. In this setting, we aim to prepare the  $\mathbb{Z}_3$  and  $\mathbb{Z}_4$  cat states:

$$|\mathbb{Z}_3\rangle = \frac{1}{\sqrt{3}} (|rgg \cdots rgg\rangle + |grg \cdots grg\rangle + |ggr \cdots ggr\rangle), \quad (\text{S21})$$

$$|\mathbb{Z}_4\rangle = \frac{1}{\sqrt{4}} (|rggg \cdots rggg\rangle + |grgg \cdots grgg\rangle + |ggrg \cdots ggrg\rangle + |gggr \cdots gggr\rangle), \quad (\text{S22})$$

starting from the product state  $|gg \cdots g\rangle$ .

Similarly to the Rydberg GHZ preparation of the main text, a natural symmetry-breaking perturbation arises here due to shot-to-shot fluctuations in the atomic positions. We incorporate these effects in the GRAPE optimization by using as a cost function the preparation fidelity averaged over  $N_s = 30$  instances of position displacements, drawn from a gaussian distribution with standard deviation  $\sigma$  (cf. Eq. (4) of the main text).

As in the main text, we set  $\Omega(t) = \Omega_0 w(t)$ , where  $w(t)$  is the cosine-tapered window function plotted in Fig. S3, with  $\alpha = 0.25$ , and use the detuning  $\Delta(t)$  as control function. In Figs. S6b and S6f, we plot the optimal cost function in the presence of positional disorder with  $\sigma = 0.03a$ , when the optimization is run with (orange line) and without positional disorder (blue line). This analysis reveals the existence of a threshold time scale  $\Omega_0 T^*$ , beyond which the optimization that accounts for symmetry-breaking perturbations identifies a protocol that mitigates preparation errors

caused by atomic position fluctuations. As shown in Figs. S6c and S6g, the resulting control profiles exhibit the characteristic features of the adiabatic echo protocol. Finally, in Figs. S6d and S6h, we demonstrate its robustness by plotting the preparation infidelity as a function of disorder strength  $\sigma$ , and comparing it to the performance of the standard adiabatic time-optimal protocol.